

# Mineralogical study and significance of the basalt-hosted Carlin-type Au deposits in southwestern Guizhou Province, China

Yuhong Yang<sup>1,2,3</sup> · Shen Liu<sup>1</sup> · Jianzhong Liu<sup>3,4,5</sup> · Zepeng Wang<sup>6</sup> ·  
Bingqiang Zhang<sup>6</sup> · Chengfu Yang<sup>6</sup>

Received: 14 May 2024 / Revised: 18 July 2024 / Accepted: 29 July 2024 / Published online: 6 September 2024

© The Author(s), under exclusive licence to Science Press and Institute of Geochemistry, CAS and Springer-Verlag GmbH Germany, part of Springer Nature 2024

**Abstract** The Jiadi and Damaidi gold deposits in southwest Guizhou Province are the largest basalt-hosted Carlin-type gold deposits recently discovered in China. This study uses the Tescan Integrated Mineral Analyzer, supported by detailed field investigations, regional geological data, and extensive sample collections, including mineralized ore, altered wall rock, and unaltered basalt samples, for ore-bearing and geochemical analyses. Comparative analysis between altered and unaltered basalt samples revealed a mineral assemblage of sericite, quartz, and pyrite. This mineral composition forms through the hydrothermal alteration of unaltered basalt, originally containing feldspar, pyroxene, and ilmenite. The wall rock primarily features sericite, quartz, and hematite. During the alteration process, major, trace, and rare earth elements notably migrate. In the Jiadi deposit, K<sub>2</sub>O, Rb, Au, and REE significantly increase, while Na<sub>2</sub>O, CaO, MgO, and MnO decrease. SiO<sub>2</sub>, Al<sub>2</sub>O<sub>3</sub>,

and Fe<sub>2</sub>O<sub>3</sub> levels remain relatively stable. In the Damaidi deposit, K<sub>2</sub>O, Rb, and Au enrich, contrasting with the depletion of Na<sub>2</sub>O, CaO, MgO, and MnO, while SiO<sub>2</sub>, Fe<sub>2</sub>O<sub>3</sub>, Al<sub>2</sub>O<sub>3</sub>, TiO<sub>2</sub>, and REE show no significant changes. In the wall rock, TiO<sub>2</sub>, Al<sub>2</sub>O<sub>3</sub>, K<sub>2</sub>O, and REE increase, while Na<sub>2</sub>O, CaO, MgO, and MnO decrease; SiO<sub>2</sub> and Fe<sub>2</sub>O<sub>3</sub> content remains unchanged. The mineralization process likely originated from mid- to low-temperature, reductive magmatic hydrothermal fluids rich in CO<sub>2</sub>, CH<sub>4</sub>, N<sub>2</sub>, H<sup>+</sup>, S<sup>2-</sup>, HS<sup>-</sup>, H<sub>3</sub>AsO<sub>3</sub>, and [Au(HS)<sub>2</sub>]<sup>-</sup>. These fluids migrated to tectonically weak zones in the Lianhuashan area, where Emeishan basalts are present. They reacted with Fe-bearing minerals in the basalt, such as ferro-hornblende and ilmenite, forming pyrite, arsenic-bearing pyrite, and arsenopyrite, thus enriching Au in these minerals. Additionally, K<sup>+</sup> and H<sup>+</sup> in the fluid reacted with plagioclase in the basalt, forming sericite and quartz. As the fluid entered the wall rock from structural weak zones, its oxidation increased, leading to the complete or partial reaction of Fe-bearing minerals in the wall rock, resulting in the formation of hematite or magnetite. This mineralization process is similar to that observed in carbonate-hosted Carlin-type gold deposits in southwest Guizhou, with the primary distinction being the iron source. In carbonate deposits, iron originates from ferridolomite within the wall rock, while in basalt-hosted deposits, it derives from ferripyroxene and ilmenite.

✉ Shen Liu  
liushen@vip.gyjg.ac.cn

Jianzhong Liu  
2585364825@qq.com

<sup>1</sup> State Key Laboratory of Continental Dynamics, Northwest University, Xi'an 710069, China

<sup>2</sup> Bureau of Land and Mineral Resources Reserve of Guizhou, Guiyang 550000, China

<sup>3</sup> Innovation Center Ore Resources Exploration Technology in the Region of Bedrock, Ministry of Natural Resources of the People's Republic of China, Guiyang 550018, China

<sup>4</sup> Guizhou Bureau of Geology and Mineral Exploration and Development, Guiyang 550004, China

<sup>5</sup> College of Resource and Environmental Engineering, Guizhou University, Guiyang 550025, China

<sup>6</sup> Geological Party 105 of the Guizhou Bureau of Geology and Mineral Exploration and Development, Guiyang, China

**Keywords** Basaltic · Ore-bearing rocks · Carlin-type · Au deposit · Mineralogy · Mineral assemblage · Element migration

## 1 Introduction

Southwestern Guizhou is a crucial area for sediment-hosted Carlin-type gold deposits in China, found in Late Paleozoic and Early Mesozoic sedimentary rocks along the southwest margin of the Precambrian Yangtze craton and the Youjiang orogenic belt (Su et al. 2018; Xie et al. 2018a). In these deposits, dolomitization is a key alteration process involving the deposition of ore pyrite. As Fe-dolomite alters to dolomite, released Fe is sulfidized, forming ore pyrite (Su et al. 2008). Recently, the Jiadi and Damaidi primary basalt-hosted Carlin-type gold deposits have been discovered in the Emeishan basalt of southwestern Guizhou Province. This discovery challenges the conventional understanding that Carlin-type gold deposits are primarily hosted in sedimentary rocks and has attracted significant attention from researchers. Researchers have primarily focused on geological and geochemical descriptions (Wu et al. 2013; Wang 2015; Wang et al. 2014; Zhang et al. 2020a, b; He et al. 2018; Zhao et al. 2018), structural analyses, sulfide chemistry, and sulfur isotope composition analyses (Li 2021; Li et al. 2021; Tian et al. 2021; Zeng et al. 2018; Zeng et al. 2014). Results indicate that the ore assemblage consists of pyrite, arsenopyrite, quartz, and clay minerals, with anomalous elements including Au, As, Hg, Tl, and Sb. The deposit formed from low-temperature (~210 °C) and low-salinity (~6.0 wt% NaCl) ore fluids. These deep ore fluids migrated vertically to the shallow crust along regional faults and then flowed horizontally into interformational fracture zones and outward into steep micro-fractures, precipitating Au. The Emeishan basalt provided both the ore-forming space and the ore-forming elements for Au mineralization. The mineral alteration process involved the transformation of orthopyroxene, plagioclase, and clinopyroxene to quartz, illite, pyrite, arsenopyrite, and (Fe)-dolomite. This study utilized traditional techniques such as scanning electron microscopy (SEM), electron probe microanalysis (EPMA), and laser ablation inductively coupled plasma mass spectrometry (LA-ICP-MS). These conventional approaches primarily focused on common regional minerals but did not analyze the combined characteristics of all minerals, especially in Carlin-type Au samples with intense alteration, diverse mineral types, complex structures, and varying sizes. Traditional light microscopes and scanning electron microscopy typically capture only localized or fragmented information, posing challenges for comprehensive, detailed, and quantitative observations of these samples. The recent introduction of the TIMA provides an innovative solution to these challenges. The TIMA system integrates scanning electron microscopy (SEM) with energy-dispersive X-ray spectrometry (EDS) to provide a quantitative analysis of rocks and minerals. The TIMA automated mineral analysis system offers a comprehensive characterization of rock samples,

including morphology, mineral classification, abundance, and distribution. It also facilitates the identification of mineral structures, association patterns, interlocking features, and inclusion relationships. Furthermore, the system enables precise localization of minor target minerals and precious metals (Chen et al. 2021). This study utilized the TIMA system to analyze ore, mineralized, altered surrounding rock, and unaltered basalt samples from the Jiadi and Damaidi basalt-hosted Carlin-type gold deposits. Through TIMA analysis, the mineral composition of various samples was obtained and compared. This comparison allows deducing the migration pattern of elements during mineralization and directly reflects the rock alteration process in these basalt-hosted Carlin-type gold deposits.

## 2 Geological setting

### 2.1 Regional geology setting

The Carlin-type gold deposits in southwestern Guizhou Province are located within the Youjiang Basin, delineated by the Mile-Shizong, Ziyun-Du'an, Honghe, and Pingxiang faults (Su et al. 2018; Xie et al. 2018a, b). The basin's evolution encompasses three stages: the passive continental margin rift basin (D1-P1), arc-back arc basin (P2-T1), and foreland basin (T2-T3) in South China (Cai and Zhang 2009; Qiu et al. 2016, 2017). This evolution corresponds to the fragmentation, subduction, and closure of the Paleo-Tethys Ocean. The collision between the South China Block and Indochina Block during the Middle-Late Triassic generated a series of NW- or NWW-striking folds and faults in the basin. In the Middle Jurassic, the subduction of the ancient Pacific plate beneath the South China plate initiated a sequence of NE-striking reverse faults and fault-propagation folds overlying the pre-existing NWW-striking structures formed during the Indosinian orogeny (Qiu et al. 2016).

The Youjiang Basin is divided by the Poping Thrust into two distinct sedimentary sequences. Northwest of the thrust, a Late Paleozoic and Triassic carbonate platform is present, while a Triassic terrigenous clastic sequence occupies the southeast. This carbonate platform contains multiple stratabound deposits within argillaceous and bioclastic limestones, and carbonate-bearing pyroclastic rocks, as seen in the Getang, Zimudan, and Shuiyindong Au deposits. In contrast, the terrigenous clastic sequence encompasses several fault-controlled deposits in calcareous sandstone and siltstone, exemplified by the Lannigou, Jinya, Banqi, and Yata deposits (Chen et al. 2011; Suo et al. 1993; Wang et al. 1994). Additionally, a variety of igneous rocks, such as Emeishan basalt, diabases, granites, quartz porphyry dikes, and alkaline ultramafic dikes, are exposed within the basin. The Upper Permian Emeishan basalt, part of the Emeishan

Large Igneous Province, surfaces along the northwestern margin of the basin and erupted about 260 million years ago, covering an area of  $> 500,000 \text{ km}^2$  (Zhou et al. 2002, 2006; Guo et al. 2004; Zhong et al. 2006). This basalt formation contains several stratabound deposits at interlayer fracture zones and interfaces with Maokou and Longtan sedimentary rocks, including the Jiadi and Damaidi deposits.

## 2.2 Geology of the Jiadi and Damaidi Au deposit

The Jiadi and Damaidi gold deposits are located along the northwestern margin of the Youjiang Basin. The Jiadi deposits have proven and probable gold resources exceeding 60 tons with an average grade of 2.0–3.0 g/ton, while the Damaidi deposit has resources of 6 tons at an average grade of 3.0–4.0 g/ton (Li et al. 2021). These deposits exhibit similar geological characteristics and are controlled by tectonic zones with multiple folds on the southeast limb of the Lianhuashan anticline. The northeast-trending Lianhuashan anticline spans approximately 10–20 km in width and 45 km in length, with both limbs dipping at low angles (Liu 2002). The northwest limb of the anticline is monocinal, whereas the southeast limb is strongly deformed and folded. The stratigraphy of these deposits includes the Middle Permian Maokou Formation, Upper Permian Longtan sedimentary rocks, and Upper Permian Emeishan basalt. Gold mineralization primarily occurs within the Emeishan basalt and at the unconformity structural alteration bodies (Shi Bian Ti, abbreviated as SBT) (Liu et al. 2010) between the Emeishan basalt/Longtan Formation and the underlying Maokou Formation. The Maokou Formation, approximately 290 m thick, is primarily composed of thick-layer limestone interbedded with dolomite and, locally, carbonaceous mudstone. The overlying Longtan Formation, mainly south of the deposit, consists predominantly of gray mudstone and siltstone, with basal layers of basalt gravel and tuff. The Emeishan basalt unconformably overlies the Maokou Formation (Fig. 1).

The volcanic succession in the Jiadi district, ranging from 150 to 350 m in thickness, is divided into three units based on lithologic characteristics. The lower unit is characterized by dark green massive basalt with interbedded dark gray tuff. The middle unit comprises gray massive basalt, basaltic tuff, and basaltic conglomerate. The upper unit primarily consists of volcanic breccia with a base of sedimentary tuff (Fig. 2). Gold mineralization at Jiadi and Damaidi is primarily strata-bound, with two layers of strata-bound orebodies identified. The upper orebody is predominantly located in the basaltic conglomerate and basaltic tuff of the middle unit of the Emeishan basalt (Fig. 3A–A'). The lower orebody is influenced by the regional SBT (Fig. 3B–B'). In this study, samples from Jiadi (JD) are derived from the upper orebody, while samples from Damaidi come from the lower orebody.

The SBT hosts several low-grade strata-bound orebodies across various gold deposits in southwestern Guizhou Province (Liu et al. 2010, 2014). The SBT has also been identified as the regional structural conduit facilitating the migration of ore fluids essential for the formation of upper gold mineralization (Liu et al. 2010, 2014; Tan et al. 2015). The primary minerals in the Jiadi gold deposit include sericite, quartz, pyrite, rutile, apatite, and pyrrhotite, while the Damaidi gold deposit includes sericite, quartz, pyrite, kaolinite, arsenopyrite, ankerite, and biotite. The ore structures are mainly volcanic breccia, with variations including layered, blocky, banded, plumose, and brecciated forms. The main alterations in the surrounding rocks include silicification, pyritization, arsenopyritization, dolomitization, clay alteration, stibnite alteration, and chloritization, with silicification, pyritization, arsenopyritization, and dolomitization most closely linked to mineralization (Li et al. 2021).

## 3 Analytical methods

### 3.1 Sample collection

In this study, altered and mineralized samples were systematically collected from the Jiadi and Damaidi gold deposits, located about 36 km southeast of Panzhou City, Guizhou Province, China. Specifically, samples JD20 and JD22 were collected from the same altered basalt breccia within the Jiadi deposit. Sample JD20 was taken from the periphery of the breccia, exhibiting more intense alteration, while JD22 was from closer to the central part of the breccia, showing less alteration. From the Damaidi deposit, ore samples (DMD13) and altered wall rock samples (DMD20) were collected; DMD13 was taken from highly altered basaltic rocks and DMD20 from an oval-shaped altered basaltic breccia forming the wall rock of the deposit. Additionally, unaltered basalt samples (XC) were collected from Xiachang Village, about 32 km southeast of the Jiadi deposit. These were taken from a large, unaltered basaltic mass. After collection, all samples were prepared into thin sections and analyzed using microscopic examination, whole-rock basic analysis, and major and trace element analysis. Additionally, mineral phase mapping of a representative sample was conducted using a Tescan Integrated Mineral Analyzer.

### 3.2 Whole-rock mineral-bearing basic analysis

Whole-rock basic analysis was performed at the Guizhou Geological and Mineral Testing center Laboratory using various specialized instruments, such as atomic fluorescence spectrometer (AFS-230ES-47), inductively coupled plasma optical emission spectrometer (Icap6300S-296),

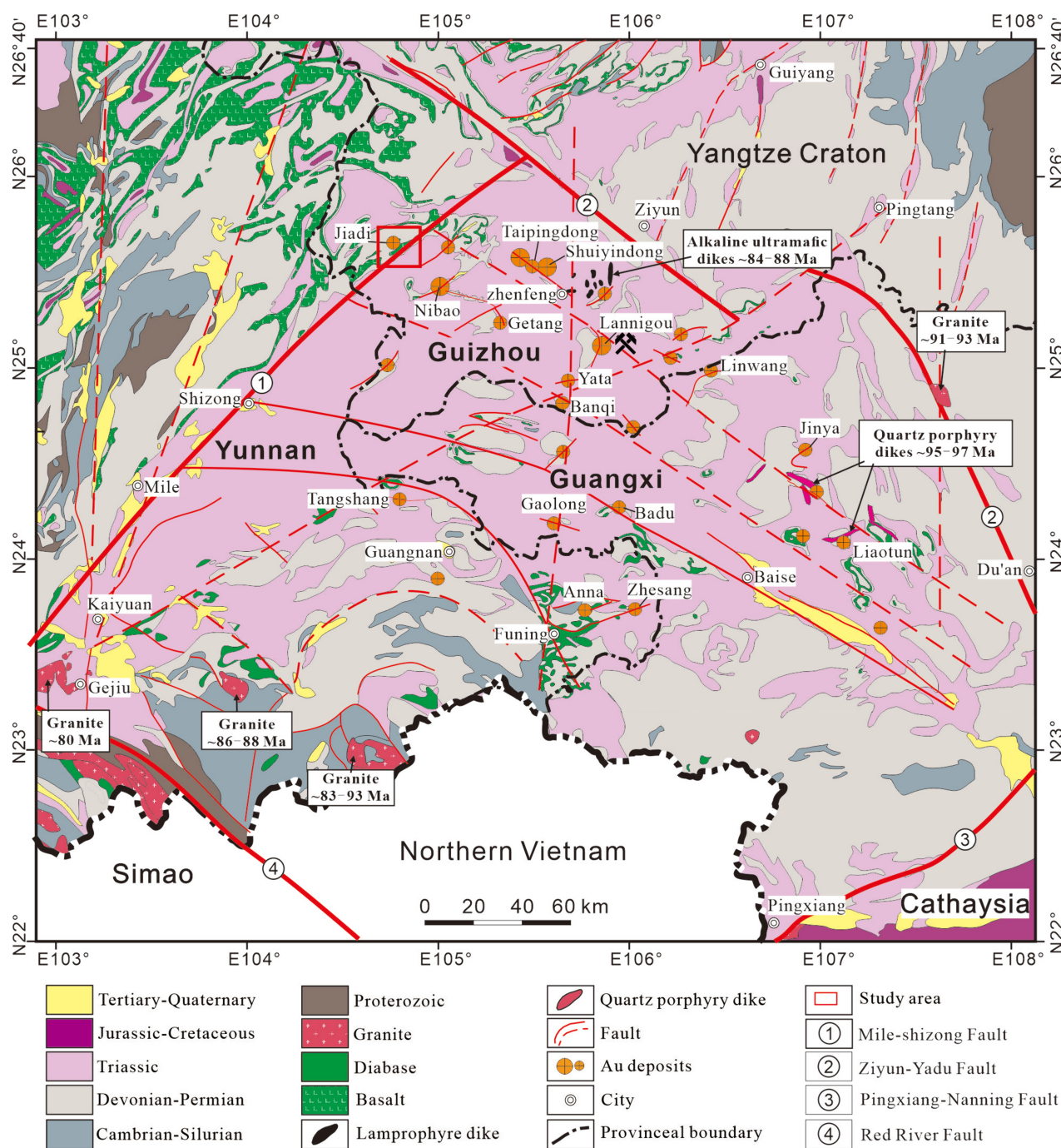


**Fig. 1** Regional geological map showing the distribution of Carlin-type Au deposits in the southwestern Guizhou Province, China (Tan et al. 2019). NCC North China Craton, IB Indo-China Block, YB Yangtze Block, CB Cathaysia Block, QL-DB Qinling Dabie, SMS Song Ma Suture

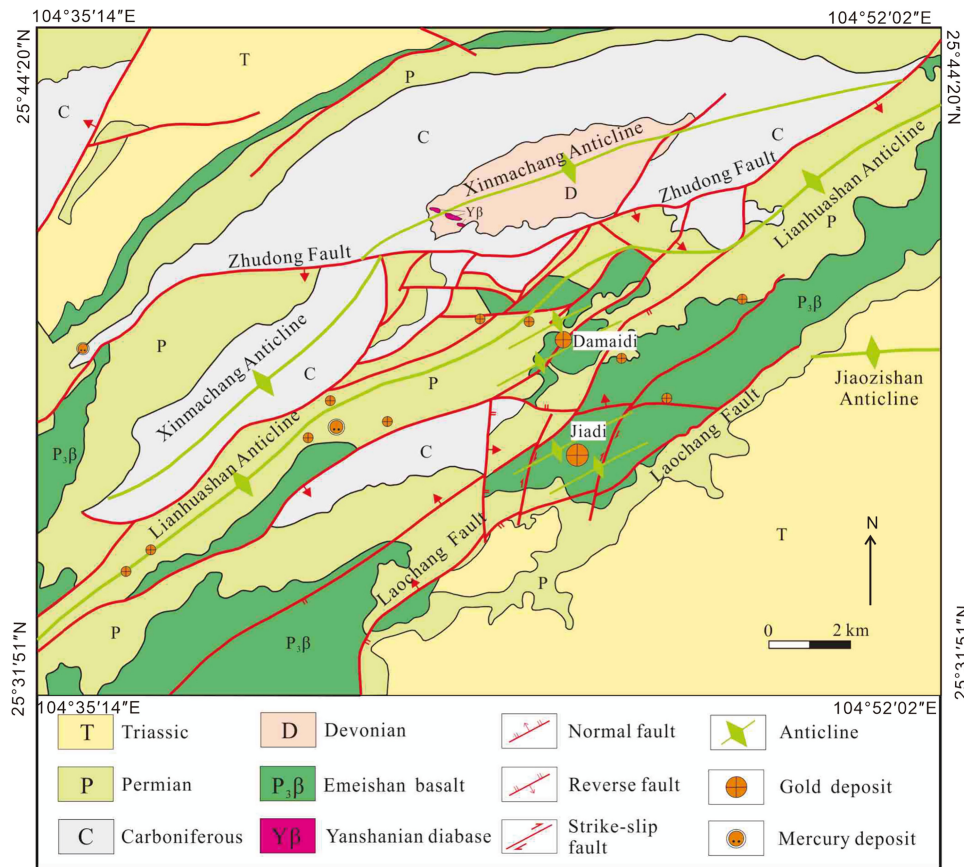
inductively coupled plasma mass spectrometry (Icapqs-319), and mercury vapor analyzer (F732-VS-479).

### 3.3 Major and trace element analysis

In this study, XC and JD22 samples were analyzed for major and trace elements at ALS Chemex (Guangzhou)

Co. Ltd., while JD20, DMD13, and DMD20 samples were analyzed at Nanjing Hongchuang Geological Exploration Technology Service Co. At ALS Chemex (Guangzhou) Co. Ltd., major elements were analyzed using an ME-XRF26d x-ray fluorescence spectrometer, with a deviation < 3.5%. Trace elements were detected using an Agilent 7700  $\times$  inductively coupled plasma mass spectrometer

**Fig. 2** Geological map of the Lianhuashan anticline illustrating the location of the Jiadi and Damaidi deposits (Li et al. 2021)



(ICP-MS), with a deviation  $< 5\%$ . At Nanjing Hongchuang Geological Exploration Technology Service Co., major elements were analyzed using x-ray fluorescence spectrometry (Shimadzu-1800), with a deviation  $< 3\%$ , and trace elements were analyzed using inductively coupled plasma mass spectrometry (ICP-MS, Agilent 7900), with a deviation  $< 5\%$ .

### 3.4 TIMA microanalysis

A TIMA at the Nanjing Hongchuang Geological Exploration Technology Service Company was used for automated mineralogical, modal, and textural analysis. Compositional maps were obtained with carbon-coated thin sections using a Mira-3 scanning electron microscope equipped with four energy-dispersive x-ray spectrometers (EDS, EDAX Element 30) (TIMA). The acceleration voltage was 25 kV, with a probe current of 9 nA. The working distance was 15 mm, with a pixel spacing of 2.5  $\mu\text{m}$  and dot spacing of 7.5  $\mu\text{m}$ . The current and BSE signal intensity were calibrated using a platinum Faraday cup with an automated procedure. EDS performance was checked using a manganese standard. The samples were scanned using the TIMA liberation analysis module.

## 4 Analysis results

### 4.1 Ore-forming element analysis

The results of the basic whole-rock analysis for this study's samples are detailed in Table 1. Samples JD20 and JD22 from the Jiadi deposit were classified as mineralized, with gold concentrations ranging from  $0.3 \times 10^{-6}$  to  $1 \times 10^{-6}$ . Conversely, sample DMD13 from the Damaidi deposit was identified as an ore sample with gold concentrations of at least  $1 \times 10^{-6}$ . Sample DMD20 was characterized as non-ore-bearing wall rock, whereas sample XC was deemed unmineralized. A positive correlation was observed between Au and As, Sb, Hg, and Tl across all samples, as shown in Table 1.

### 4.2 Major element analysis results

The results of the major element analysis for an average of mineralized samples JD, ore sample DMD13, and wall rock sample DMD20 compared with unmineralized sample XC (Table 2) show similar SiO<sub>2</sub> (43.6%, 43.6%, 46.8% vs. 46%), TiO<sub>2</sub> (4.24%, 2.94%, 4.42% vs. 3.07%), and Fe<sub>2</sub>O<sub>3</sub>T (15.7%, 14.9%, 16.3% vs. 15.6%) but with different MnO (0.02%, 0.15%, 0.07% vs. 0.24%). They also show higher K<sub>2</sub>O

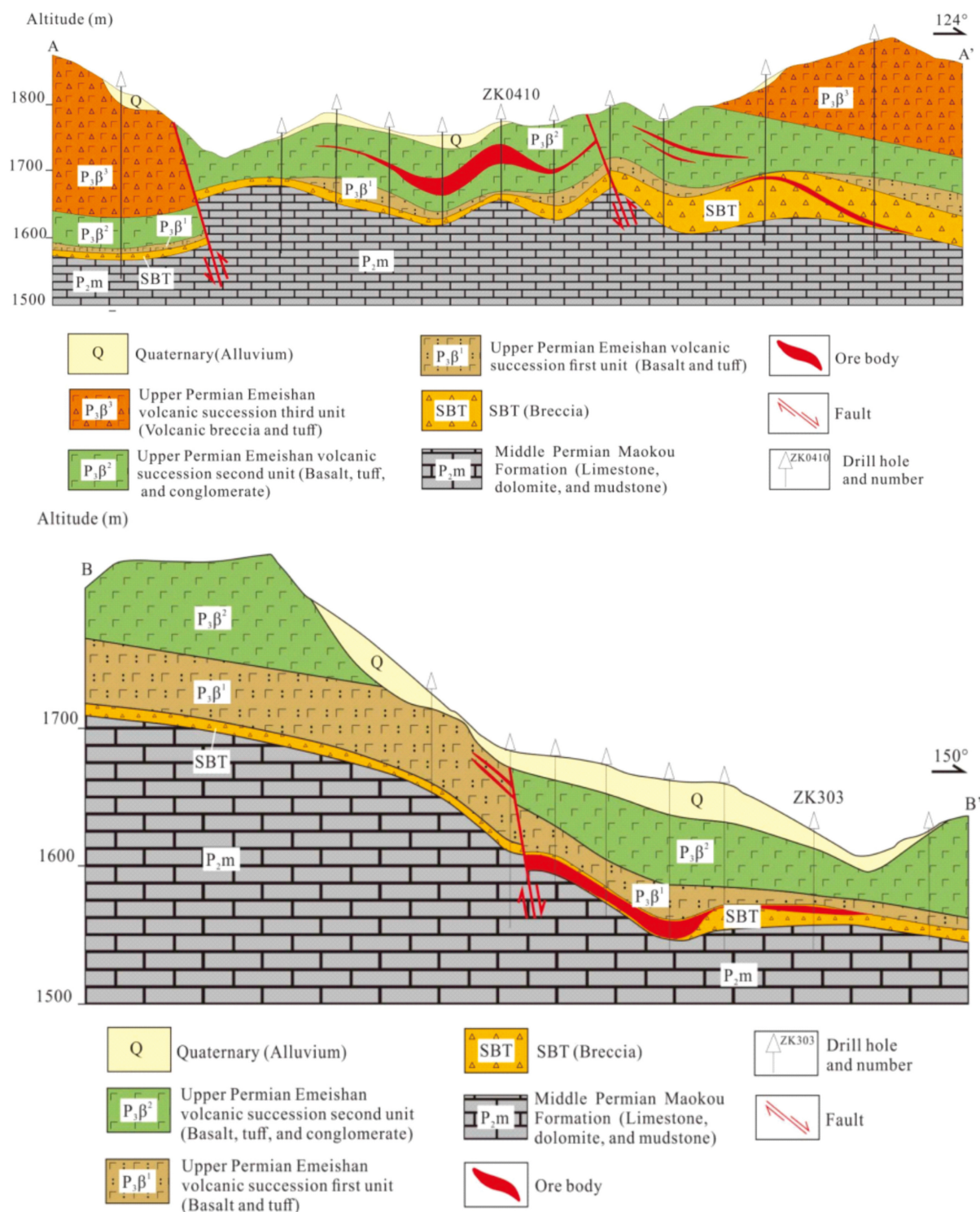


**Fig. 3** Geological cross section of exploration line in Jiadi (A–A') and Damadi (B–B') deposit (Li et al. 2021)

(3.88%, 2.75%, 1.2% vs. 0.24%) and lower MgO (0.49%, 2.85%, 0.83% vs. 5.78%), CaO (2.12%, 4.19%, 1.94% vs. 9.98%), and Na<sub>2</sub>O (0.04%, 0%, 0.02% vs. 2.84%). Additionally, JD has higher P<sub>2</sub>O<sub>5</sub> (1.78%) than DMD and XC (Table 2).

#### 4.3 Trace element analysis results

Plotting the samples on primitive mantle-normalized multi-element variation diagrams (normalized to the primitive mantle composition of Sun and McDonough 1989) indicates

**Table 1** Ore-forming element analysis data of samples (unit:  $10^{-6}$ )

Sample no.	Au	As	Sb	Hg	Tl
JD20	0.41	11,209	60.3	6.51	6.64
JD22	0.31	1234	20.6	7.55	6.52
DMD13	5.64	17,885	39.5	1.20	6.46
DMD20	0.03	61.3	11.1	0.07	1.05
XC	0.04	11.9	0.67	0.09	0.14

**Table 2** Whole rock major element analysis results (wt%)

Sample no.	JD	DMD13	DMD20	XC-4
SiO <sub>2</sub>	43.6	43.6	46.8	46.0
TiO <sub>2</sub>	4.24	2.94	4.42	3.07
Al <sub>2</sub> O <sub>3</sub>	15.1	12.0	19.9	14.1
Fe <sub>2</sub> O <sub>3</sub> <sup>T</sup>	15.7	14.9	16.3	15.6
MnO	0.02	0.15	0.07	0.24
MgO	0.49	2.85	0.83	5.78
CaO	2.12	4.19	1.94	9.98
Na <sub>2</sub> O	0.04	0.00	0.02	2.84
K <sub>2</sub> O	3.88	2.75	1.20	0.82
P <sub>2</sub> O <sub>5</sub>	1.78	0.34	0.77	0.56
LOI	12.0	14.4	7.94	1.42
Sum	99.0	98.1	100.2	100.4

the Jiadi (JD) and Damaidi (DMD) samples are depleted in large ion lithophile element (LILE, Ba and Sr) relative to the unaltered basaltic rock sample XC but are immobile in the high field strength elements (HFSE, e.g., Nb, Ta, Zr, Hf, and Th) (Table 3; Fig. 4A). The samples contain elevated total REE contents (XC, 175 ppm; JD20, 343 ppm; JD22, 296 ppm; DMD13, 132 ppm; DMD20, 354 ppm) and have chondrite-normalized REE variation diagram patterns (normalized to the chondrite composition of Sun and McDonough 1989) that slope down to the right, indicating they are enriched in light REE (LREE) but depleted in heavy REE (HREE) (Fig. 4B). They have LREE/HREE ratios of XC, 7.42; JD20, 6.85; JD22, 6.03; DMD13, 7.10; DMD20, 9.09.

#### 4.4 TIMA liberation analysis results

This study based on TIMA liberation analysis was conducted on a representative sample to accurately identify its mineral assemblages and texture characteristics (Table 4; Fig. 5).

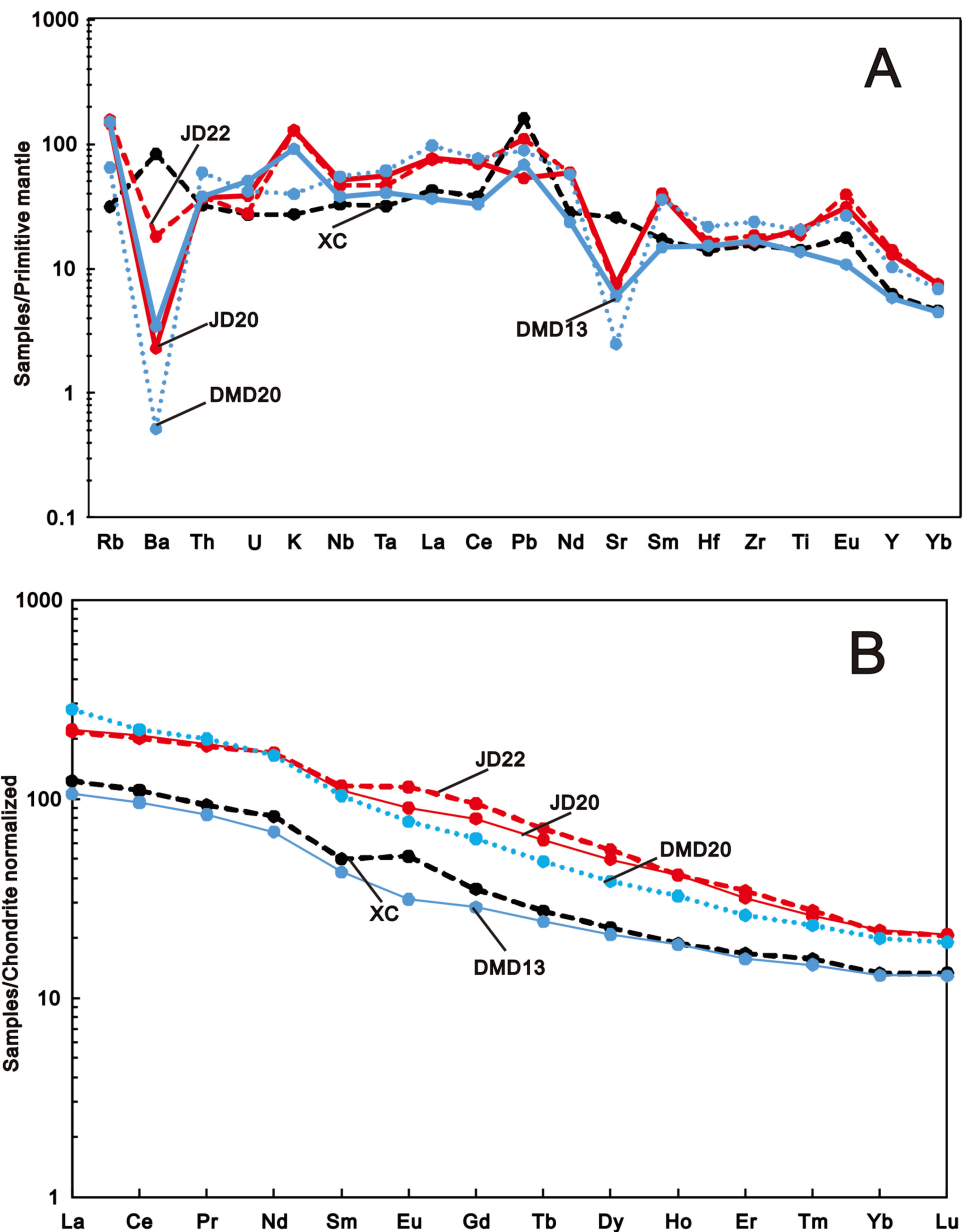
The results show that samples JD20 and JD22 are dominated by sericite (31.0% and 26.5%), quartz (24.0% and 27.2%), and pyrite (24.4% and 23.2%), altered phase (Ti) (7.91% and 7.08%), altered phase (3.31% and 5.0%), followed by rutile (4.55% and 4.54%) and apatite (0.54% and 3.06%). Sample DMD13 is dominated by sericite (19.8%), quartz (25.7%), and pyrite (18.5%), with Ti (11.0%) and

**Table 3** Whole rock trace element analysis results (unit:  $10^{-6}$ )

Sample no.	JD20	JD22	DMD13	DMD20	XC-4
Rb	93.0	99.5	95.8	41.0	19.9
Ba	16.0	127	24.0	3.60	581
Th	3.12	3.21	3.23	5.04	2.73
U	0.81	0.58	1.07	0.88	0.57
Nb	37.0	33.2	27.1	39.1	23.4
Ta	2.28	1.90	1.66	2.51	1.30
La	52.6	51.4	25.1	66.7	29.2
Ce	128	123	58.6	136	67.4
Pr	17.9	17.5	7.91	19.0	8.8
Sr	161	147	127	52.3	543
Nd	78.9	79.6	31.9	77.1	38.1
Zr	184	207	188	266	174
Hf	4.71	5.10	4.72	6.70	4.30
Sm	16.9	17.8	6.55	15.8	7.6
Eu	5.22	6.64	1.81	4.46	2.98
Gd	16.3	19.4	5.86	12.9	7.22
Tb	2.32	2.65	0.90	1.81	1.02
Dy	12.6	14.1	5.27	9.77	5.71
Y	58.7	64.4	26.4	46.7	28.3
Ho	2.33	2.35	1.05	1.84	1.06
Er	5.26	5.71	2.59	4.30	2.76
Tm	0.66	0.70	0.37	0.59	0.40
Yb	3.71	3.65	2.20	3.38	2.25
Lu	0.53	0.52	0.33	0.48	0.34
$\Sigma$ REE	175	343	345	150	354
LREE	154	299	296	132	319
HREE	20.8	43.7	49.0	18.6	35.1
LREE/HREE	7.42	6.85	6.03	7.10	9.09

altered phase (9.02%), followed by ankerite (5.74%), arsenopyrite (2.89%), and kaolinite (2.20%) (Table 4). The arsenopyrite clusters predominantly exhibit grain sizes ranging from approximately 30 to 200  $\mu\text{m}$ , while ankerite occupies cracks and kaolinite exhibits a planar pattern (Fig. 6 DMD13). Sample DMD13 is dominated by sericite (19.8%), quartz (25.7%), and pyrite (18.5%), with Ti (11.0%) and another altered phase (9.02%), followed by ankerite (5.74%), arsenopyrite (2.89%), and kaolinite (2.20%) (Table 4). The arsenopyrite clusters predominantly exhibit grain sizes ranging from approximately 30 to 200  $\mu\text{m}$ , while ankerite occupies cracks and kaolinite shows a planar pattern (Fig. 6 DMD13). Sample XC is dominated by plagioclase (40.2%) and anorthoclase (8.1%), diopside (23.8%), ferrosilite (6.03%), chlorite-(Fe) (9.94%), and ilmenite (7.66%) (Table 4). The ferropyroxene is surrounded by ferrochlorite, indicating that the formation of ferrochlorite is a result of the alteration of ferropyroxene. The sericite exhibits an oriented or semi-oriented arrangement with grain sizes while retaining the morphological characteristics of plagioclase observed in the

**Fig. 4** Chondrite-normalized REE diagrams (**A**) and primitive mantle-normalized spider diagrams (**B**)



basalt. The irregular spaces between the sericite structures were occupied by quartz and pyrite grains, with quartz also filling bands and cracks. Rutile and Ti appeared in a point-like distribution throughout the scanned area, indicating that the Ti may consist of ilmenite grains that have not fully altered.

## 5 Discussion

### 5.1 Transformation law of minerals during hydrothermal alteration

The TIMA analysis demonstrates that three types of samples from the Jiadi and Damaidi deposits, including

unaltered basalt samples, have revealed significant transformations in mineral composition across the ore district. The basaltic rocks, originally composed of plagioclase, pyroxene, and ilmenite, underwent hydrothermal alteration resulting in the formation of rocks containing sericite, quartz, and other minerals. The ore and mineralized samples primarily consist of sericite, quartz, and pyrite, with ore samples exhibiting higher concentrations of arsenopyrite, ferridolomite, and kaolinite. Conversely, mineralized samples contain higher concentrations of minerals such as rutile, apatite, and pyrrhotite. The wall rock mainly consists of sericite and quartz but is devoid of pyrite, containing higher levels of hematite (magnetite) and calcite compared to the ore-bearing samples (Fig. 5). Fluid

**Table 4** Various mineral phases identified on study samples using (TIMA) technique

Database (%)	JD-20		JD-22		DMD-13		DMD-20		XC	
	Mass	Volume	Mass	Volume	Mass	Volume	Mass	Volume	Mass	Volume
Sericite	31.0	35.3	26.5	30.0	19.8	21.9	35.9	38.4	0	0
Quartz	24.1	29.0	27.2	32.5	25.7	30.1	18.5	20.9	0	0
Pyrite	24.4	15.4	23.2	14.6	18.5	11.4	0	0	0	0
Altered phase-(Ti)	7.91	8.66	7.08	7.64	11.0	11.8	11.7	11.6	0	0
Altered phase	3.31	3.48	5	5.23	9.02	9.74	9.13	9.02	0	0
Rutile	4.55	3.38	4.54	3.35	0.58	0.42	3.46	2.42	0	0
Hematite/magnetite	0.04	0.02	0	0	0.05	0.03	10.9	6.31	0	0
Kaolinite	0.1	0.12	0.08	0.09	2.2	2.6	5.48	6.25	0	0
Ankerite	0	0	0	0	5.74	5.95	1.8	1.79	0	0
Orthoclase	2.22	2.74	1.96	2.4	2.37	2.84	0	0	0	0
Apatite	0.54	0.54	3.06	3.05	0.03	0.03	0.01	0.01	1.16	1.09
Arsenopyrite	0.01	0	0	0	2.89	1.46	0	0	0	0
Pyrrhotite	1.37	0.95	0.39	0.27	0.92	0.61	0	0	0	0
Calcite	0	0	0	0	0	0	2.53	2.77	0	0
Biotite	0.27	0.27	0.65	0.66	0.32	0.32	0.04	0.03	1.01	0.97
Hornblende	0	0	0	0	0.66	0.7	0.04	0.04	0	0
Baryte	0.09	0.06	0.33	0.23	0.01	0.01	0	0	0	0
Schorl	0	0	0	0	0	0	0.28	0.26	0	0
Diopside	0	0	0	0	0.13	0.02	0	0.1	0	0
Plagioclase	0	0	0	0	0.02	0.13	0.09	0	0	0
Ilmenite	0	0	0	0	0	0	0.09	0.06	0	0
Orthopyroxene	0	0	0	0	0	0	0.07	0.06	0	0
Zircon	0.01	0.01	0.01	0.01	0	0	0	0	0	0
Anorthite	0	0	0	0	0	0	0.01	0.01	0	0
Zoisite-(Fe)	0	0	0	0	0	0	0	0	0	0
Titanite	0	0	0	0	0	0	0	0	0	0
Albite	0	0	0	0	0	0	0	0	0	0
Chlorite-(Mg)	0	0	0	0	0	0	0	0	0	0
Plagioclase	0	0	0	0	0	0	0	0	40.2	44.5
Diopside	0	0	0	0	0	0	0	0	23.8	21.7
Chlorite-(Fe)	0	0	0	0	0	0	0	0	9.94	11.1
Anorthoclase	0	0	0	0	0	0	0	0	8.10	9.34
Ilmenite	0	0	0	0	0	0	0	0	7.66	4.80
Ferrosilite	0	0	0	0	0	0	0	0	6.03	4.60
Zoisite	0	0	0	0	0	0	0	0	0.96	0.86
Olivine (Mg, Fe)	0	0	0	0	0	0	0	0	0.92	0.84
Titanite	0	0	0	0	0	0	0	0	0.08	0.07
Hyalophane	0	0	0	0	0	0	0	0	0.01	0.01
[Unclassified]	0.06	0.07	0	0	0.01	0.02	0.03	0.04	0.11	0.11
Total	100	100	100	100	100	100	100	100	100	100

metasomatism affects both the wall rock and ore-bearing rock in the Jiadi and Damaidi mining areas. Notably, sericitization occurs in both contexts, while pyritization is restricted to ore-bearing rock. The presence of pyrrhotite in the mineralized sample indicates a lower iron content during alteration compared to that in the ore. Additionally, the presence of magnetite in the wall rock suggests more

pronounced oxidation of the alteration fluid compared to that within the deposit.

## 5.2 Migration of elements during hydrothermal alteration

Previous studies have optimized the mass balance method for tracking element migration (Grant 1986, 2005), indicating

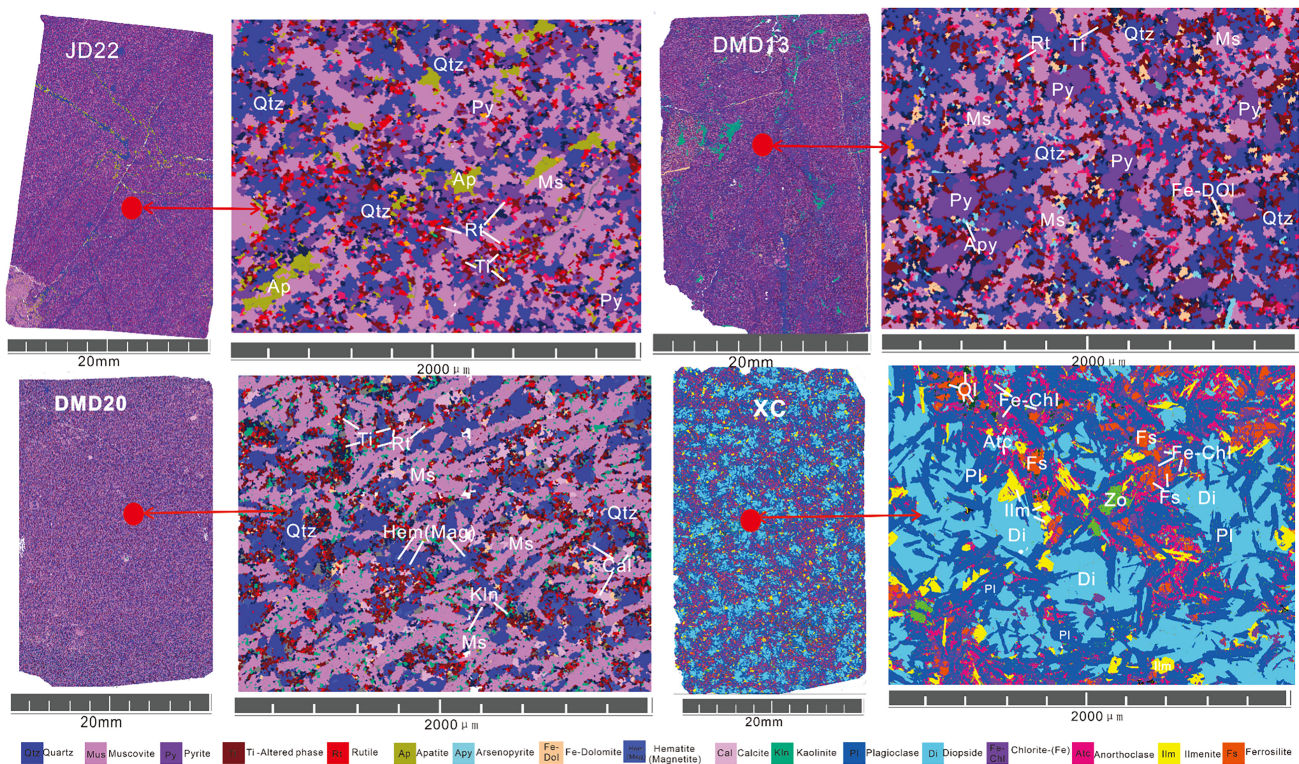


**Fig. 5** Mineral assemblages and texture characteristics of TIMA liberation analysis images from study area

that the degree of element migration can be quantified by the ratio of the change in element mass to its initial mass before alteration ( $\Delta C_i/C_i^0$ ). This study evaluates the  $\Delta C_i/C_i^0$  ratios from unaltered basalt XC to altered rocks JD and DMD, and from unaltered wall rock DMD20 to ore-bearing altered rocks JD and DMD13, as shown in Table 5 and Fig. 6. In altered sample JD, elements such as K<sub>2</sub>O, P<sub>2</sub>O<sub>5</sub>, TiO<sub>2</sub>, Au, Rb, and REEs show increased concentrations compared to unaltered basalt XC. In contrast, the concentrations of Na<sub>2</sub>O, CaO, MgO, MnO, and Sr decrease, while the levels of SiO<sub>2</sub>, Al<sub>2</sub>O<sub>3</sub>, and Fe<sub>2</sub>O<sub>3</sub>T remain relatively unchanged. Sample DMD13 shows an influx of K<sub>2</sub>O, Au, and Rb and a significant efflux of Na<sub>2</sub>O, CaO, MgO, MnO, Al<sub>2</sub>O<sub>3</sub>, and Sr. The concentrations of SiO<sub>2</sub>, Fe<sub>2</sub>O<sub>3</sub>T, TiO<sub>2</sub>, and REEs remain relatively stable. The alterations in DMD20 are consistent with those in the Jiadi samples, except for the efflux of Au.

### 5.3 Element migration patterns during hydrothermal alteration of minerals

The hydrothermal alteration process is the mechanism of mineral metasomatism (Yu et al. 2020). The mineral assemblages of samples JD20, JD22, and DMD13 indicate

that the dominant alteration process involves plagioclase, anorthoclase, diopside, ferrosilite, chlorite-(Fe), and ilmenite in basalt transforming into sericite, quartz, and pyrite in altered rocks. Under the influence of potassium-rich fluids, plagioclase (or anorthoclase) alters into sericite and quartz. As mentioned earlier, Na<sub>2</sub>O, CaO, and MgO were effluxed, and K<sup>+</sup> was influxed, while Fe<sub>2</sub>O<sub>3</sub>T and SiO<sub>2</sub> remained unchanged (Fig. 6). This suggests that the fluid carries away the remaining Na<sup>+</sup>, Ca<sup>2+</sup>, and Mg<sup>2+</sup> and brings in K<sup>+</sup> during the conversion process of plagioclase to sericite while also altering the pyroxene. Fe in pyrite within mineralized rocks primarily originates from Fe-bearing minerals present in basaltic rocks, such as ferropyroxene (ferrochlorite) and ilmenite. In a reduction environment, these minerals lead to the generation of Fe<sup>2+</sup>, while in an oxidation environment, Fe-bearing minerals in wall rock generate Fe<sup>3+</sup> (hematite or magnetite). Quartz is derived from SiO<sub>2</sub> produced by these aforementioned reactions rather than from fluid. The mechanisms underlying elemental migration are outlined as follows:

1. Plagioclase (or anorthoclase) undergoes sericite formation:

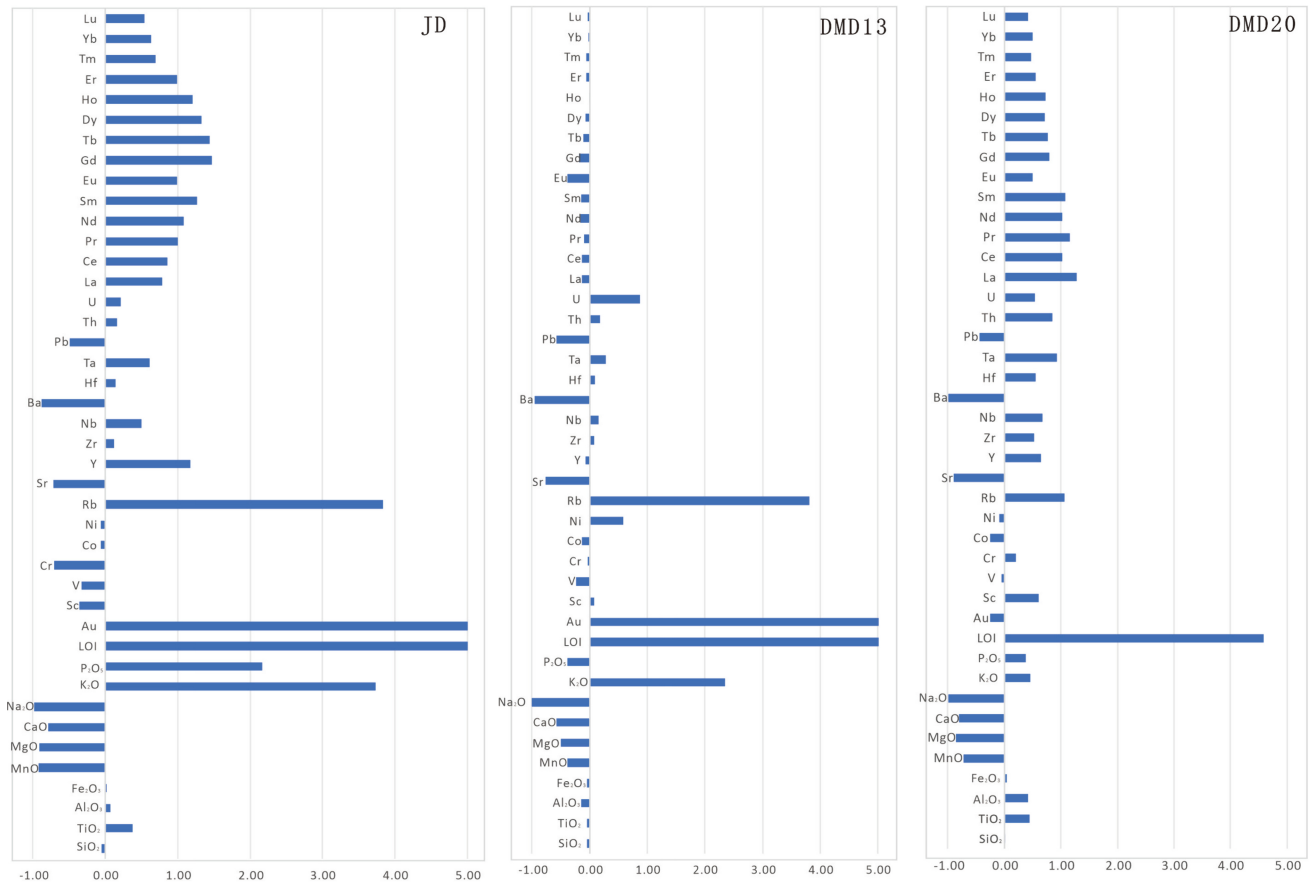
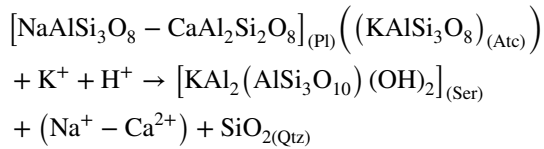
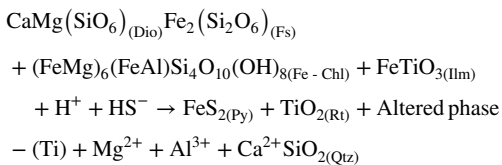


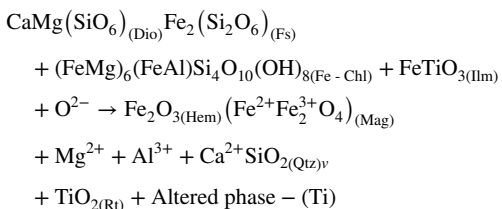
**Fig. 6**  $\Delta C_i/C_i^0$  Diagram of the altered rock and unaltered basalt



## 2. Chlorite-(Fe) and ilmenite undergo pyrite formation:



## 3. Hydrothermal alteration in the wall rock:



## 5.4 The mechanism of mineral precipitation

Previous studies have shown that the ore-forming hydrothermal fluids in this research area are characterized by a reducing environment, primarily consisting of elements such as  $\text{K}^+$ ,  $\text{H}^+$ ,  $\text{S}^{2-}$ ,  $\text{HS}^-$ ,  $\text{Au}$ ,  $\text{As}$ ,  $\text{Sb}$ ,  $\text{Hg}$ ,  $\text{Tl}$ ,  $\text{H}_3\text{AsO}_3$ , and  $[\text{Au}(\text{HS})_2]^-$  (Li et al. 2021; Tian 2021; Du et al. 2020; Min 2021; Jun et al. 2017). These fluids, enriched with  $\text{H}_3\text{AsO}_3$ ,  $[\text{Au}(\text{HS})_2]^-$ ,  $\text{S}^{2-}$ , and  $\text{HS}^-$ , interact with iron-bearing minerals in the basalts of the Emeishan volcanic rocks in the Lianhuashan area. This interaction leads to the sulfidation of iron-bearing minerals such as chlorite and ilmenite, resulting in the formation of pyrite, arsenopyrite, and quartz. Notably,  $\text{Au}$  becomes enriched in arsenopyrite and pyrite during this process (Hofstra and Cline 2000, 2005). As the reducing reactions progress, the consumption of  $\text{S}^{2-}$ ,  $\text{HS}^-$ ,  $\text{H}_3\text{AsO}_3$ , and  $[\text{Au}(\text{HS})_2]^-$  leads to a gradual transition of the fluid from a reducing to an oxidizing state. The reaction of hydrothermal fluids containing  $\text{K}^+$  and  $\text{H}^+$  with plagioclase (or anorthoclase) results in the formation of sericite and quartz. As  $\text{HS}^-$  ions decrease, the reducibility of the fluid diminishes, resulting

**Table 5**  $\Delta C_i$  and  $(\Delta C_i/\text{CO}_i)$  values of the altered rock and unaltered basalt

Element	$\Delta C_{i\text{JD-XC}}$	$\Delta C_{i\text{JD}}/C_{i\text{XC}}^0$	$\Delta C_{i\text{DMD13-XC}}$	$\Delta C_{i\text{DMD13}}/C_{i\text{XC}}^0$	$\Delta C_{i\text{DMD20-XC}}$	$\Delta C_{i\text{DMD20}}/C_{i\text{XC}}^0$
$\text{SiO}_2$	-2.41	-0.05	-2.42	-0.05	0.80	0.02
$\text{TiO}_2$	1.17	0.38	-0.13	-0.04	1.35	0.44
$\text{Al}_2\text{O}_3$	1.05	0.07	-2.14	-0.15	5.81	0.41
$\text{Fe}_2\text{O}_3$	0.12	0.01	-0.67	-0.04	0.73	0.05
$\text{MnO}$	-0.22	-0.92	-0.09	-0.38	-0.18	-0.73
$\text{MgO}$	-5.29	-0.92	-2.93	-0.51	-4.96	-0.86
$\text{CaO}$	-7.86	-0.79	-5.79	-0.58	-8.04	-0.81
$\text{Na}_2\text{O}$	-2.81	-0.99	-2.84	-1	-2.82	-0.99
$\text{K}_2\text{O}$	3.06	3.73	1.93	2.35	0.38	0.46
$\text{P}_2\text{O}_5$	1.22	2.17	-0.22	-0.39	0.21	0.38
LOI	10.5	7.42	13.0	9.17	6.52	4.59
Total	-1.43	-0.01	-2.28	-0.02	-0.19	0
Au	0.32	8.00	5.6	140	-0.01	-0.25
Sc	-9.03	-0.36	1.95	0.08	15.07	0.6
V	-152	-0.33	-105.43	-0.23	-21.5	-0.05
Cr	-71.1	-0.71	-3.57	-0.04	19.7	0.2
Co	-4.8	-0.06	-10.6	-0.14	-19.6	-0.25
Ni	-7.95	-0.07	69	0.59	-11	-0.09
Rb	76.4	3.84	75.9	3.81	21.1	1.06
Sr	-389	-0.72	-416	-0.77	-491	-0.9
Y	33.3	1.18	-1.92	-0.07	18.4	0.65
Zr	21.7	0.12	14.0	0.08	91.9	0.53
Nb	11.7	0.5	3.7	0.16	15.7	0.67
Ba	-510	-0.88	-557	-0.96	-577	-0.99
Hf	0.61	0.14	0.42	0.1	2.40	0.56
Ta	0.79	0.61	0.36	0.28	1.21	0.93
Pb	-5.61	-0.49	-6.54	-0.57	-5.09	-0.45
Th	0.44	0.16	0.5	0.18	2.31	0.85
U	0.12	0.22	0.5	0.87	0.31	0.54
La	22.8	0.78	-4.1	-0.14	37.5	1.28
Ce	58.0	0.86	-8.84	-0.13	68.8	1.02
Pr	8.86	1	-0.91	-0.1	10.2	1.15
Nd	41.2	1.08	-6.23	-0.16	39.0	1.02
Sm	9.7	1.27	-1.09	-0.14	8.2	1.07
Eu	2.95	0.99	-1.17	-0.39	1.48	0.5
Gd	10.6	1.47	-1.36	-0.19	5.72	0.79
Tb	1.47	1.44	-0.12	-0.11	0.79	0.77
Dy	7.61	1.33	-0.44	-0.08	4.06	0.71
Ho	1.28	1.21	-0.01	-0.01	0.78	0.73
Er	2.73	0.99	-0.17	-0.06	1.54	0.56
Tm	0.28	0.7	-0.03	-0.07	0.19	0.47
Yb	1.43	0.63	-0.05	-0.02	1.13	0.5
Lu	0.18	0.54	-0.01	-0.04	0.14	0.42

in its penetration into the wall rock through a structurally weak zone. The elliptical basalt breccia in the wall rock facilitates surface water infiltration, significantly intensifying the oxidation process. When encountering oxidizing conditions within the wall rock, this fluid interacts with iron-bearing minerals such as ferropyroxene (ferrichlorite)

and ilmenite, resulting in the formation of hematite or magnetite. Similar ore-forming processes are observed in the carbonate-hosted mining areas of southwest Guizhou Province, such as the Shuiyindong deposit. However, variations in the host rocks lead to differences in the types of hydrothermal alterations, with decarbonation and

sulfidation reactions predominating in carbonate-hosted mining areas (Su et al. 2009).

## 6 Conclusion

- This study reveals a positive correlation between Au content and the elements As, Sb, Hg, and Tl in altered samples. Major element analysis shows that  $\text{SiO}_2$  and  $\text{Fe}_2\text{O}_3\text{T}$  contents are similar to those in unaltered basalt for both ore and mineralized samples, whereas  $\text{K}_2\text{O}$  content is elevated and  $\text{Na}_2\text{O}$  content is reduced compared to unaltered basalt. Trace element analysis indicates a depletion of large ion lithophile elements, Ba and Sr, in the Jiadi and Damaidi samples relative to the unaltered basaltic rock sample XC. However, high field strength elements (Nb, Ta, Zr, Hf, and Th) remain immobile. Additionally, the REE patterns display an enrichment of LREEs and a depletion of HREEs across all samples. The REE content in the Jiadi mineralized samples and the surrounding rocks of Damaidi is higher than in unaltered basalt but lower compared to Damaidi ore samples.
- Mineralogically, the area transitions from basaltic rocks containing plagioclase, pyroxene, and ilmenite to altered rocks predominantly composed of sericite and quartz. Within ore or mineralized rocks, sericite, quartz, and pyrite dominate, whereas wall rocks are primarily composed of sericite, quartz, hematite (magnetite), and calcite.
- The mineralization process in the area is inferred to have originated from a mid- to low-temperature, reductive magmatic hydrothermal fluid rich in  $\text{CO}_2$ ,  $\text{CH}_4$ ,  $\text{N}_2$ ,  $\text{H}^+$ ,  $\text{S}^{2-}$ ,  $\text{HS}^-$ ,  $\text{H}_3\text{AsO}_3$ , and  $[\text{Au}(\text{HS})_2]^-$ . This fluid migrated to tectonically weak zones in the Lianhuashan area where Emeishan basalts are distributed. The fluid, containing  $\text{H}_3\text{AsO}_3$ ,  $[\text{Au}(\text{HS})_2]^-$ ,  $\text{S}^{2-}$ , and  $\text{HS}^-$ , reacted with Fe-bearing minerals in the basalt such as ferro-hornblende (ferro-actinolite) and ilmenite to form pyrite, arsenic-bearing pyrite, and arsenopyrite, while Au was enriched in arsenic-bearing pyrite and arsenopyrite. Additionally,  $\text{K}^+$  and  $\text{H}^+$  in the fluid reacted with plagioclase (anorthoclase) in basalt to form sericite and quartz. As the fluid entered the wall rock from the structural weak zone, the elliptical basalt breccia in the wall rock facilitated surface water infiltration, significantly intensifying the oxidation process. When encountering oxidizing conditions within the wall rock, this fluid interacts with iron-bearing minerals such as ferripyroxene (ferrichlorite) and ilmenite, resulting in the formation of hematite or magnetite.
- The mineralization process is similar to that of carbonate-hosted Carlin-type gold deposits in southwest Guizhou. However, the Fe source in carbonate deposits

originates from minerals like ferridolomite within the wall rock, whereas in basalt-hosted Carlin-type gold deposits, Fe derives from ferripyroxene (ferrichlorite), ilmenite, and other minerals.

**Acknowledgements** We thank No. 105 Geological Team of the Guizhou Bureau of Geology and Mineral Exploration & Development for conducting the field work.

**Author contributions** Conceptualization, SL and JL; validation, SL and JL; methodology, YY; software, YY; formal analysis, YY, ZW; samples collection, JL, YY, ZW, BZ and CY.

**Funding** This study was jointly funded by the Talent Team Program of Science and Technology Foundation of Guizhou Province (CXTD [2021]007), the Key Project of Natural Science Basic Research Program of Shanxi Province (2023-JC-ZD-16), the National Natural Science Fund of China (U1812402), the National Key Research and Development Program of China “Exploration and Exploitation of Deep Earth Resources” (2017YFC0601500), the National Natural Science Fund of China (41962008), and the Guizhou Province Graduate Research Fund (YJSCXJH [2020]095), and the public welfare and fundamental project Fund of Guizhou Province (520000214 TLCOG7DGTNRG).

## Declarations

**Conflict of interest** The authors declare no conflict of interest.

## References

- Cai JX, Zhang KJ (2009) A new model for the Indochina and South China collision during the Late Permian to the Middle Triassic. *Tectonophysics* 467:35–43.
- Chen MH, Mao JW, Bierlein FP, Norman T, Uttley PJ (2011) Structural features and metallogenesis of the Carlin-type Jinfeng (Lannigou) gold deposit, Guizhou Province, China. *Ore Geol Rev* 43:217–234.
- Chen Q, Song WL, Yang JK, Hu Y, Huang J, Zhang T, Zhang GS (2021) Principle of automated mineral quantitative analysis system and its application in petrology and mineralogy: An example from TESCAN TIMA. *Miner Depos* 40:345–368.
- Du ZZ, Cheng ZZ, Yao XF, Yu XF, Chen H, Li SH, Bao XL (2020) Element migration regularity during hydrothermal alteration in the Xiejiagou gold deposit, Eastern Shandong Province. *Geol Bull China* 39:1137–1152.
- Grant JA (1986) The isogon diagram: A simple solution to Gresens' equation for metasomatic alteration. *Econ Geol* 81:1976–1982.
- Grant JA (2005) Isogon analysis: A brief review of the method and applications. *Phys Chem Earth Parts A/B/C* 30:997–1004.
- Guo F, Fan WM, Wang YJ, Li CW (2004) When did the Emeishan mantle plume activity start? Geochronological and geochemical evidence from ultramafic-mafic dikes in Southwestern China. *Int Geol Rev* 46:226–234.
- He JP, Yuan SF, Wang XY, Pin HY (2018) Geochemical characteristics of the Lianhuashan Anticline in the Southwest Guizhou Dense Area of Mineral Deposits, 2018. *J Sichuan Geol* 38:384–387 (**in Chinese with English abstract**).

- Hofstra AH, Cline JS (2000) Characteristics and models for Carlin type gold deposits. *Rev Econ Geol* 66:163–220.
- Hofstra AH, Emsbo P, Christiansen WD, Theodorakos P, Zhang XC, Hu RZ, Su WC, Fu SH (2005) Source of ore fluids in Carlin-type gold deposits, China: Implications for genetic models. Springer, Berlin.
- Li JH (2021) The study of ore-forming processes of the Jiadi and Damaidi basalt-hosted gold deposits, southwestern Guizhou Province, China. Ph.D. Thesis, College of Resources and Environmental Engineering, Guizhou University, Guiyang, China, pp 1–122.
- Li JH, Wu P, Xie ZJ, Liu JZ, Zhang SJ, Song WF, Zhang BQ, Li ST, Xu LY, Zheng LL (2021) Alteration and paragenesis of the basalt-hosted Au deposits, southwestern Guizhou Province, China: implications for ore genesis and exploration. *Ore Geol Rev* 131:104034.
- Liang DP, Yang WX, Wang JB, Tang XL, Ariser S (2017) Early to Middle Triassic sedimentary records in the Youjiang Basin, South China: Implications for Indosinian orogenesis. *J Asian Earth Sci* 141:125–139.
- Liu YH (2002) Analysis on the minerogenetic geological condition of the gold ore in the Lianhuashan anticline, western Guizhou. *Guizhou Geol* 19:231–234 (in Chinese with English abstract).
- Liu JZ, Yang CF, Xia Y, Chen S, Chen FE, Fu ZK (2010) SBT study and ideas in platform facies area in the southwest Guizhou. *Guizhou Geol* 27:178–184 (in Chinese with English abstract).
- Liu JZ, Xia Y, Tao Y, Yang CF, Wang ZP, Tan QP, Fu SH, Chen R, Wu WM (2014) The relation between SBT and gold-antimony deposit metallogenesis and prospecting in southwest Guizhou. *Guizhou Geol* 31:267–272 (in Chinese with English abstract).
- Liu JZ, Wang ZP, Yang CF, Li JH, Zheng LL, Chen FE, Xu LY, Song WF, Wang DF, Tan QP, Xie ZJ, Song WF, Xu LY, Li ST, Wang DF, Qin YJ, Liu JK, Yang YH, Wang XY (2022) Discriminant index and significance of structural body Altera-Tion of Carlin-type gold deposits in Yunnan-Guizhou-Guangxi and its surrounding areas, China. *Gold Sci Technol* 30:532–539.
- Min Z (2021) Metallogenesis of the Jiadi Golden Deposit in Southwestern Guizhou Province. M.D. Thesis, A Dissertation submitted to East China University of Technology, pp 1–42.
- Qiu L, Yan DP, Tang SL, Wang Q, Yang WX, Tang X, Wang J (2016) Mesozoic geology of southwestern China: Indosinian foreland overthrusting and subsequent deformation. *J Asian Earth Sci* 122:91–105.
- Su WC, Xia B, Zhang HT, Zhang XC, Hu RZ (2008) Visible gold in arsenian pyrite at the Shuiyindong Carlin-type gold deposit, Guizhou, China: Implications for the environment and processes of ore formation. *Ore Geol Rev* 33:667–679.
- Su WC, Heinrich CA, Pettke T, Zhang XC, Hu RZ, Xia B (2009) Sediment-hosted gold deposits in Guizhou, China: Products of wall-rock sulfidation by deep crustal fluids. *Econ Geol* 104:73–93.
- Su WC, Dong WD, Zhang XC, Shen NP, Hu RZ, Hofstra, AH, Cheng LZ, Xia Y, Yang KY (2018) Carlin-type gold deposits in the Dian-Qian-Gui “golden triangle” of southwest China. In: Muntean JL (ed) Diversity in Carlin-style gold deposits. Rev. Econ. Geol. 20. Society of Economic Geologists Inc., Littleton, pp 157–185.
- Sun SS, McDonough WF (1989) Chemical and isotopic systematics of oceanic basalts: implications for mantle composition and processes. In: Saunders AD, Norry MJ (eds) Magmatism in the ocean basins 42. Geol Soc Lond Spec Publ, pp 313–345.
- Suo ST, Hou GG, Zhang MF, Wang K (1993) The large Panjiang river multi-level sheeted thrust-nappe structure in southwestern Guizhou. *Reg Geol China* 3:239–247 (in Chinese with English abstract).
- Tan QP, Xia Y, Xie ZJ, Yan J (2015) Migration paths and precipitation mechanisms of ore-forming fluids at the Shuiyindong Carlin-type gold deposit, Guizhou. *China Ore Geol Rev* 69:140–156.
- Tan QP, Xia Y, Xie ZJ, Yan J, Wang ZP, Wei DT, Zhao YM, Yan J, Li ST (2019) Two hydrothermal events at the Shuiyindong Carlin-type gold deposit in Southwestern China: Insight from Sm–Nd dating of fluorite and calcite. *Minerals* 2019(9):230.
- Tian C (2021) Characteristics of gold-bearing Pyrite from the Jiadi gold deposit in southwestern Guizhou and its implications for mineralization. M.D. Thesis, Chang'an University, Xi'an, China, pp 1–63.
- Wang DF (2015) A preliminary study on the geological and geochemical characteristics of the Jiadi gold deposit in Panxian, Guizhou. M.thesis, Guiyang, China, Guizhou University, p 66 (in Chinese with English abstract).
- Wang YG, Suo ST, Zhang MF (1994) Structure and Carlin-type gold deposit in Southwestern Guizhou, vol 86. Geological Publishing House, Beijing (in Chinese with English abstract).
- Wu XH, Cheng PL, Xiao CG, Ma J (2013) Metallogenic geologic characteristics of Damaidi gold deposit in basalt distribution area of Western Guizhou. *Guizhou Geol* 30:283–288 (in Chinese with English abstract).
- Xie ZJ, Xia Y, Cline JS, Koenig A, Wei DT, Tan QP, Wang ZP (2018a) Are there Carlin-type Au deposits in China? A comparison between the Guizhou China and Nevada USA deposits. In: Muntean JL (ed) Diversity in Carlin-style gold deposits. Rev. Econ. Geol. 20. Society of Economic Geologists Inc., Littleton, pp 187–233.
- Xie ZJ, Xia Y, Cline JS, Pribil MJ, Koenig A, Tan QP, Wei DT, Wang ZP, Yan J (2018b) Magmatic origin for sediment-hosted Au deposits, Guizhou Province, China: In situ chemistry and sulfur isotope composition.

Springer Nature or its licensor (e.g. a society or other partner) holds exclusive rights to this article under a publishing agreement with the author(s) or other rightsholder(s); author self-archiving of the accepted manuscript version of this article is solely governed by the terms of such publishing agreement and applicable law.